AGU PUBLICATIONS

JGR

Journal of Geophysical Research: Oceans

RESEARCH ARTICLE

10.1002/2014JC009792

Key Points:
- RIS basal melt rates near ice front factor of 10 larger than ice-shelf average
- Near-ice-front basal melt rates depend similarly on tidal and subtidal currents
- Modeling predicts maximum near-ice-front basal melt rates in austral summer

Supporting Information:
- Description of auxiliary material
- Tables

Correspondence to:
R. C. Beardsley,
rbeardsley@whoi.edu

Citation:
Arzeno, I. B., R. C. Beardsley, R. Limeburner, B. Owens, L. Padman, S. R. Springer, C. L. Stewart, and M. J. M. Williams (2014), Ocean variability contributing to basal melt rate near the ice front of Ross Ice Shelf, Antarctica, *J. Geophys. Res. Oceans*, *119*, 4214–4233, doi:10.1002/2014JC009792.

Received 3 JAN 2014
Accepted 4 JUN 2014
Accepted article online 10 JUN 2014
Published online 9 JUL 2014

Ocean variability contributing to basal melt rate near the ice front of Ross Ice Shelf, Antarctica

Isabella B. Arzeno[1], Robert C. Beardsley[2], Richard Limeburner[2], Breck Owens[2], Laurie Padman[3], Scott R. Springer[4], Craig L. Stewart[5,6], and Michael J. M. Williams[5]

[1]Department of Civil and Environmental Engineering, Stanford University, Stanford, California, USA, [2]Woods Hole Oceanographic Institution, Woods Hole, Massachusetts, USA, [3]Earth & Space Research, Corvallis, Oregon, USA, [4]Earth & Space Research, Seattle, Washington, USA, [5]National Institute of Water and Atmospheric Research, Wellington, New Zealand, [6]Now at Scott Polar Research Institute, Cambridge University, Cambridge, UK

Abstract Basal melting of ice shelves is an important, but poorly understood, cause of Antarctic ice sheet mass loss and freshwater production. We use data from two moorings deployed through Ross Ice Shelf, ~6 and ~16 km south of the ice front east of Ross Island, and numerical models to show how the basal melting rate near the ice front depends on sub-ice-shelf ocean variability. The moorings measured water velocity, conductivity, and temperature for ~2 months starting in late November 2010. About half of the current velocity variance was due to tides, predominantly diurnal components, with the remainder due to subtidal oscillations with periods of a few days. Subtidal variability was dominated by barotropic currents that were large until mid-December and significantly reduced afterward. Subtidal currents were correlated between moorings but uncorrelated with local winds, suggesting the presence of waves or eddies that may be associated with the abrupt change in water column thickness and strong hydrographic gradients at the ice front. Estimated melt rate was $\sim 1.2 \pm 0.5$ m a^{-1} at each site during the deployment period, consistent with measured trends in ice surface elevation from GPS time series. The models predicted similar annual-averaged melt rates with a strong annual cycle related to seasonal provision of warm water to the ice base. These results show that accurately modeling the high spatial and temporal ocean variability close to the ice-shelf front is critical to predicting time-dependent and mean values of meltwater production and ice-shelf thinning.

1. Introduction

The Antarctic Ice Sheet (AIS) consists of grounded ice, some of which rests on a bed that is well below sea level, and ice shelves that are the floating extensions of grounded glaciers and ice streams flowing across the grounding line. The mass budget of the grounded portion of the Antarctic Ice Sheet is dominated by input from snow and loss through lateral ice mass flux across the grounding line into the ocean. The present ice sheet mass balance is negative, largely due to a recent acceleration in dynamic mass loss along the ocean margins of the West Antarctic Ice Sheet (WAIS) [*Shepherd et al*., 2012]. While the present rate of WAIS mass loss is small, equivalent to ~0.2 mm a^{-1} of global sea level rise [*Shepherd et al*., 2012], there is evidence that a large fraction of the WAIS was lost in some previous interglacial climates [*Naish et al*., 2009].

Pollard and DeConto [2009] modeled the behavior of Antarctica's ice sheets over the past 5 million years, concluding that the disappearance of the WAIS was correlated with an ocean-driven long-term retreat of ice shelves in the Ross, Weddell, and Amundsen seas. These results, and several observational and regional modeling studies [e.g., *Scambos et al*., 2004; *Dupont and Alley*, 2005; *Joughin et al*., 2010], suggest that ice shelves regulate the loss of grounded ice through a process referred to as "buttressing", in which friction at the ice-shelf margins opposes the flow of glaciers and ice streams delivering grounded ice to the ocean. If ice shelves retreat or thin, net frictional stresses are reduced, and accelerated ice sheet mass loss to the ocean may occur. Given evidence that some Antarctic ice shelves are presently losing mass quite rapidly [*Pritchard et al*., 2012; *Rignot et al*., 2013], understanding the mechanisms causing this mass loss is essential for projecting the contribution of the AIS to global sea level change over the next several decades to centuries.

The mass budget of an ice shelf is determined by the gains by ice inflow across the grounding line, direct precipitation to the ice-shelf surface and losses through iceberg calving and basal melting as relatively

warm ocean water circulates underneath it. (For some ice shelves, surface melting and drainage may also contribute to net mass loss.) Here we focus on basal melting, which accounts for about half the net loss of ice for Antarctic ice shelves [*Rignot et al*., 2013; *Depoorter et al*., 2013]. Basal melt rates depend on ocean temperature and boundary layer current velocities [*Lewis and Perkin*, 1986; *Holland and Jenkins*, 1999]. Elevation of ocean temperature above the in situ freezing point provides the heat required for the phase transition from ice to liquid water. Currents under the ice-shelf erode stratification by inducing turbulence that maintains the upward flux of subsurface ocean heat to the ice base, and by flushing away the cold, buoyant meltwater that would otherwise impede further ocean heat flux to the ice.

Time-averaged ice-shelf melt rate, $w_b(\mathbf{x})$, around Antarctica is highly heterogeneous [*Shepherd et al*., 2010; *Rignot et al*., 2013; *Depoorter et al*., 2013], ranging from ice-shelf-averaged values of $\sim$0.1 m a^{-1} for the large ice shelves to $>$10 m a^{-1} for some of the smaller ice shelves in the Amundsen Sea. The larger values occur where warm water masses such as relatively unmodified Circumpolar Deep Water (CDW; $T > 1°$C) intrude across the continental shelf then under the ice shelves [*Pritchard et al*., 2012]. For these ice shelves, currents just below the ice base are usually dominated by the thermohaline circulation driven by the buoyancy flux from ice melt. Smaller values of basal melt rate are found where thermal forcing is small (i.e., the water is cold). For these ice shelves, the thermohaline circulation is generally weak, and other sources of ocean currents such as tides become important; see *MacAyeal* [1984a, 1984b], *Makinson et al*. [2011], and *Mueller et al*. [2012] for modeling studies of the Ross Ice Shelf (RIS), Filchner-Ronne Ice Shelf (FRIS), and Larsen C Ice Shelf, respectively. For each of these ice shelves, most of the water entering the sub-ice-shelf cavity is near the surface freezing point of seawater ($T_f(S,P=0) \sim -1.9°$C for typical salinities of $S = 34.5$), and tidal current speeds can greatly exceed the flows driven by other mechanisms.

Although all large ice shelves that are underlain by cold water are presently close to steady state [*Pritchard et al*., 2012; *Rignot et al*., 2013], modeling by *Hellmer et al*. [2012] suggests that changes in global climate may lead to more rapid mass loss from FRIS later in the 21st century. While these authors suggested that RIS is more stable than FRIS to projected climate change, there is considerable uncertainty in the characteristics of 21st century climate projections that ultimately affect basal mass loss: when the paleo evidence for RIS variability [*Naish et al*., 2009; *Pollard and DeConto*, 2009] is also considered, we assume that RIS may also be at risk over timescales of a century or longer. However, although we can estimate recent values of $w_b(\mathbf{x})$ from satellite altimetry and other data sets [e.g., *Horgan et al*., 2011; *Pritchard et al*., 2012; *Rignot et al*., 2013], our understanding of the actual processes that determine $w_b(\mathbf{x})$ under RIS is poor. Therefore, we cannot yet estimate future melt rates even if we could accurately forecast large-scale changes in the background ocean state from global coupled climate models.

Only a few direct observations of ocean variability have been made under RIS. Hydrographic profiles over an interval of several hours were obtained at site J9 in the southeastern RIS during the Ross Ice Shelf Project [*Gilmour*, 1979; *Jacobs et al*., 1979; *Foster*, 1983]. More recently, time series data have been obtained south of Ross Island. *Robinson et al*. [2010] obtained a 23 day record under land-fast sea ice in McMurdo Sound in 2003, and shorter records (of $\sim$2 day and $\sim$4 day duration) at two sites under McMurdo Ice Shelf. *Tyler et al*. [2013] and *Stern et al*. [2013] obtained a 6 month record of the ocean temperature profile in 2011–2012, also under McMurdo Ice Shelf; however, they did not record contemporaneous currents. No records, to date, have obtained simultaneous time series of all the variables needed to estimate basal melt rates under RIS for a period that is sufficiently long to resolve ocean processes expected to contribute significantly to melt rate variability.

In this paper, we report on measurements of temperature, salinity, and currents collected under RIS during a $\sim$2 month period from late November 2010 to late January 2011 (during the transition from austral spring to summer). These data were obtained from the Coulman High site, near the RIS ice front east of Ross Island (Figure 1), to help design future ANDRILL drilling operations (http://andrill.org/science/ch). We use this data set to investigate the causes and energetics of sub-ice-shelf ocean currents and hydrographic variability close to the ice-shelf edge, and their roles in basal melting. We augment these analyses with a coupled ocean/ice-shelf model to estimate the annual cycle of basal melting and investigate the role of tides in melting near the ice front.

The paper is organized as follows. Section 2 describes the moorings and supporting GPS and atmospheric data. Section 3 summarizes the numerical models. Section 4 presents the tidal analysis of the mooring and

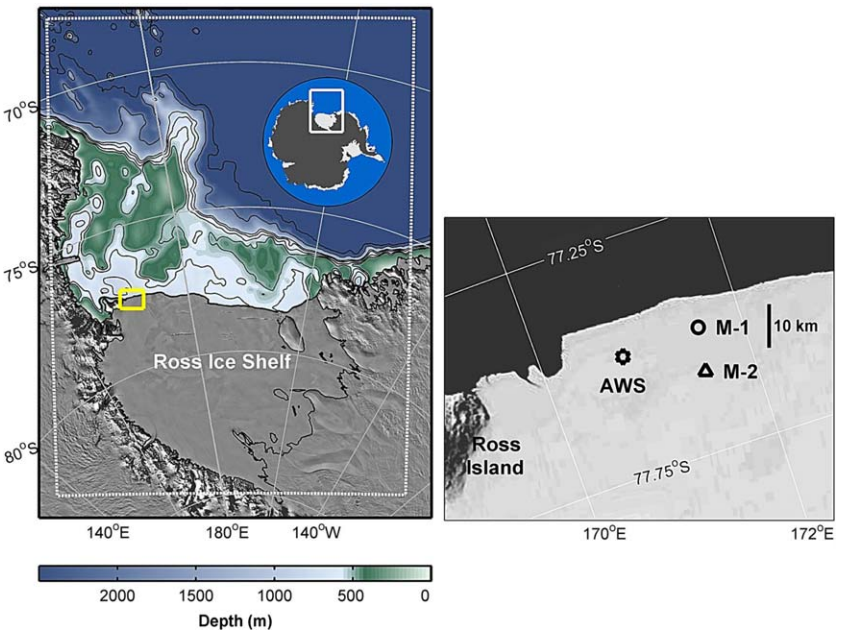

Figure 1. (left) Ross Ice Shelf (RIS) and Ross Sea, Antarctica. Background grayscale image is from MODIS Mosaic of Antarctica (MOA) [*Scambos et al*., 2007]. Filled contours north of the ice front show water depth (color scale (m) at bottom of plot). Yellow box on northwest RIS indicates Coulman High site east of Ross Island. White-dashed rectangle denotes ROMS model domain. (right) Expanded view of ANDRILL region, showing locations of mooring M-1 (deployed by NIWA) and M-2 (deployed by WHOI) deployed through the ice shelf (see section 2 and Table 1 for more details). M-1 is about 6 km from the ice-shelf edge and about 10 km north of M-2. Location of Automatic Weather Station (AWS) "Laurie II" is also shown. Background image is MODIS Aqua for 13 February 2011.

GPS records. Section 5 describes the subtidal variability. Section 6 presents estimates of basal melting. Section 7 discusses variability of melting over a wide range of time scales and identifies processes that need to be considered in assessing net melting. Our findings are summarized in section 8.

2. Measurements

Two sites, M-1 and M-2, were occupied ~6 and ~16 km south of the RIS ice front, respectively, during the late spring and early austral summer of 2010–2011 (Table 1 and Figure 1). Measurements included time series of ice-shelf surface elevation from GPS receivers and sub-ice-shelf water properties from moored sensors. Total ice thickness was 262 and 273 m at M-1 and M-2, respectively.

Near-surface wind velocity ($\mathbf{U}_W$), air temperature (T_{air}), and pressure (P_{air}) data (Figures 2a–2c) were collected at automatic weather station (AWS) "Laurie II" (77.4961°S, 170.7892°E), deployed about 19 km west of M-1 by the Antarctic Meteorological Research Center (U. Madison-Wisconsin). The basic meteorological data collected during the mooring deployment period were edited to produce hourly data for analysis.

GPS receivers were deployed at both mooring sites to record ice-shelf surface elevation (z_{GPS}) and lateral motion (not discussed here). The GPS at M-1 recorded data every 15 s from 9 November 2010 to 18 January 2011 (70 days), and the M-2 GPS recorded data every 30 s from 14 November 2010 to 9 July 2011 (237 days). Data were processed using the approach of *King et al*. [2011a, 2011b], with ocean tide loading

Table 1. ANDRILL Mooring Locations, Deployment Periods, and Site Conditions[a]

	Latitude (S)	Longitude (E)	Distance From Ice Edge (km)	Start Time (UTC)	End Time (UTC)	Bottom of Ice Shelf (m)	Seafloor Bottom (m)	Water Column Thickness (m)
M-1	77°29.3′	171°34.3′	~6	24 Nov 2010	17 Jan 2011[b]	219.0	798.5	579.5
M-2	77°34.9′	171°30.4′	~16	2 Dec 2010	23 Jan 2011	228.0	862.0	634.0

[a]All depths presented in this paper are expressed as meters below mean sea level.
[b]The shallowest M-1 Aquadopp finished measuring prematurely on 13 January 2011 (19:56:13).

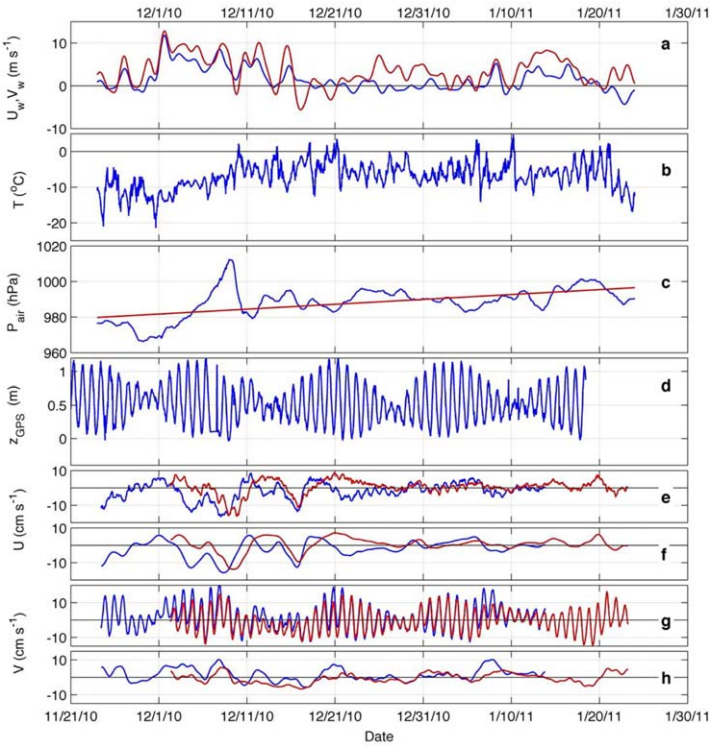

Figure 2. Time series showing AWS Laurie II meteorological data, the M-2 GPS data, and the M-1 and M-2 depth-averaged current data. (a) Eastward U_w (blue) and northward V_w (red) wind components (m s^{-1}); (b) air temperature T (°C); (c) air pressure P_{air} (hPa); (d) GPS ice height z_{GPS} (m) adjusted for the IBE due to the linear trend in P_{air}; (e) basic and (f) low-pass filtered depth-averaged M-1 (red) and M-2 (blue) eastward current components U (cm s^{-1}); and (g) basic and (h) low-pass filtered M-1 (red) and M-2 (blue) northward current components V (cm s^{-1}). The linear trend in P_{air} is shown as a red line in plot (c).

displacements computed with the SPOTL package [*Agnew*, 1996, 1997] applied to the TPXO6.2 ocean tide model [*Egbert and Erofeeva*, 2002]. The GPS data (Figure 2d) were interpolated and low-pass filtered with a 4 h filter to reduce noise, then averaged with a 30 min boxcar filter every 30 min. The values of z_{GPS} were adjusted to account for the inverse barometer effect (IBE), in which a 1 hPa increase in P_{air} depresses the sea surface height (and surface of the overlying, hydrostatically floating, ice shelf) by ~0.01 m [*Chelton and Enfield*, 1986; *Padman et al*., 2003]. We used the time series of P_{air}, low-passed with a cutoff of 0.5 cycles per day (cpd) to estimate the IBE; see *Padman et al*. [2003] for an explanation of the choice of cutoff frequency. This procedure removes most of the apparent trend in z_{GPS} associated with the trend in P_{air} of ~0.27 hPa d^{-1} (Figure 2c).

Moorings (see schematics in Figure 3) were deployed by melting holes through the ice shelf with a hot-water drill. Ocean current velocities (**u**) were measured using Nortek Aquadopps. Conductivity (*C*) and temperature (*T*) were measured using Seabird Electronics SBE-38 Microcats (Table 2). On M-1, **u**(*t*) was recorded as 5 min averages every 10 min, and *C*(*t*) and *T*(*t*) were spot-sampled every 10 min. On M-2, 6 min averaged values of **u**(*t*) were obtained every 30 min, and *C*(*t*) and *T*(*t*) were spot-sampled every 7.5 min.

The M-1 current meter data were first interpolated, using a cubic spline method, over gaps longer than 10 min and then subsampled every 30 min. Depth-averaged velocity components for the M-1 and M-2 currents were estimated using linear interpolation in the vertical. Bad data were removed from the Microcat time series when effects from the ice hole on the instrument were evident, or if the instrument was frozen over. The Microcat data were averaged using a 30 min boxcar window. The combined 30 min edited data records were then low-passed filtered using the PL66 filter with a 33 h half-amplitude period [*Beardsley and Rosenfeld*, 1983] before being used for the subtidal portion of this study. The basic and low-pass filtered, depth-averaged, east and north current components are shown in Figures 2e–2h.

Conductivity-Temperature-Depth (CTD) profiles were made with a pumped Seabird Electronics SBE19plus lowered through the hole before and after the M-1 deployment and before the M-2 deployment (Table 3 and

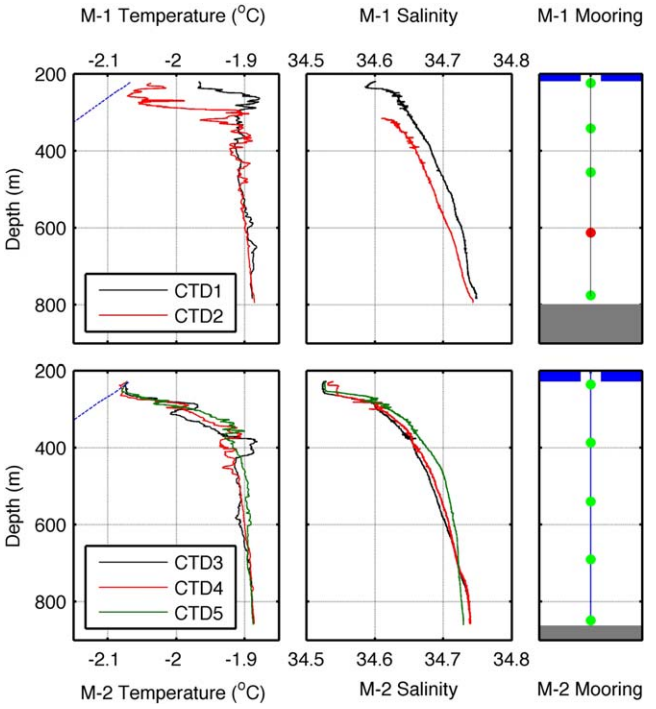

Figure 3. Vertical profiles of the CTD temperature and salinity data recorded at the M-1 and M-2 mooring sites in the left two columns and the vertical distribution of the M-1 and M-2 instrumentation in the right column (Table 2). Top two plots show the M-1 CTD1 and CTD2 data, lower two plots the M-2 CTD3, CTD4, and CTD5 data. See Table 3 for the cast times and depth of casts. The blue-dashed line in the left plots indicates the freezing temperature of sea water as a function of in situ salinity and pressure. The blue and gray-shaded areas at the top and bottom of the right plots indicate the ice shelf and ocean bottom, respectively. A current meter and Microcat were deployed at each green dot while only a current meter was deployed at the red dot on M-1.

Figure 3). All profiles showed a layer of cold, relatively fresh water just below the ice, with *T* and salinity (*S*) increasing with depth toward the bottom. The largest difference between profiles occurred between the pre and postdeployment casts (CTD-1 and CTD-2) at M-1, which were separated by ~58 days. The three predeployment casts at M-2 exhibited smaller differences ($|\delta T| < 0.03^{\circ}$C; $|\delta S| < 0.03$). The top ~20 m of the water column at M-2 was at or very close to the in situ freezing temperature $T_f(S,P)$.

3. Numerical Models

Two numerical models were used: the Circum-Antarctic Tidal Simulation inverse barotropic tide model, version 2008 (CATS2008), and the Regional Ocean Modeling System (ROMS) [*Shchepetkin and McWilliams*, 2005].

The CATS2008 model, which has 4 km grid spacing on a polar stereographic grid, is an update of the inverse tide model described by *Padman et al*. [2002]. Assimilated data in the Ross Sea include: coastal tide gauges in McMurdo Sound and Terra Nova Bay; gravimeter, GPS and satellite laser altimeter data collected on RIS [*Padman et al*., 2008]; and a bottom pressure record near Cape Adare [*Padman et al*., 2009]. The GPS data collected at the Coulman High site were not assimilated into CATS2008.

The ROMS model solves the three-dimensional equations of motion with the hydrostatic and Boussinesq approximations and includes a thermodynamically active ice shelf; see *Dinniman et al.* [2007] for a detailed description of the model components. Our configuration was based on a recent version used to study the Ross Sea [*Dinniman et al*., 2011]. The model equations were solved on a uniform lateral grid with spacing between nodes of 5 km in the domain shown in Figure 1. Bathymetry and ice-shelf draft were obtained from the original BEDMAP product [*Lythe et al*., 2001]; see *Dinniman et al*. [2007] for further information. The model used a 24 level terrain-following vertical coordinate system that improves model representation of processes near lower and upper boundaries, including the sloping base of the ice shelf. Some smoothing of the BEDMAP grids was required to satisfy numerical stability issues in ROMS; see *Mueller et al*., [2012],

Table 2. ANDRILL Moored Instrument Depths

Aquadopp Depth (m)		Microcat Depth (m)	
M-1	M-2	M-1	M-2
226.4	236.0	224.4	236.0
343.4	390.0	341.4	386.5
457.4	543.0	455.4	540.0
612.4	691.0	775.4	690.0
777.4	851.5		848.5

Table 3. CTD Cast Locations, Time, and Maximum Depth of Cast

CTD	Site	Date	Max. Depth (m)
1	M-1	22 Nov 2010	782.7
2	M-1	18 Jan 2011	793.8
3	M-2	29 Nov 2010	855.7
4	M-2	30 Nov 2010	856.7
5	M-2	1 Dec 2010	858.9

Table 4. Values Used to Infer P_1 and K_2 From the ANDRILL M-2 GPS Record (238 Day Record Length)[a]

Constituent	Frequency (cycles h^{-1})	Amplitude (m)	Phase[a] (°)
P_1	0.0415526	0.077	200.4
K_1	0.0417807	0.237	196.7
K_2	0.0835615	0.012	307.7
S_2	0.0833333	0.033	305.8

[a]Phase given in degrees relative to Greenwich.

supporting information for a detailed description of grid-smoothing constraints. This smoothing, particularly of ice-shelf draft, can influence ocean circulation and basal melting, as discussed in subsequent sections.

In ocean regions free of sea ice, surface fluxes were calculated from daily-averaged atmospheric variables taken from the Antarctic Mesoscale Prediction System (AMPS), a mesoscale atmospheric forecast model [*Bromwich et al.*, 2005]. In regions covered by sea ice, surface fluxes were calculated using a coupled sea ice model [*Budgell*, 2005] rather than being specified from satellite observations as done by *Dinniman et al.* [2011]. Turbulent heat and salt fluxes beneath the ice shelf were calculated as functions of the time-varying friction velocity [*Holland and Jenkins*, 1999; *Dinniman et al.*, 2011].

The model runs were designed to support studies of sea-ice response to ocean tides [*Mack et al.*, 2013], and so do not overlap the present measurement period. We ran four simulations: 2 year integrations (17 September 2003 to 11 September 2005) with output averaged over 5 days, without and with tidal forcing; and 6 month runs (19 December 2004 to 17 June 2005) with output averaged over 4 h, without and with tidal forcing. For tidal forcing, we specified CATS2008 elevations and normal barotropic velocities along the open boundaries [see *Mueller et al.*, 2012]; the direct astronomical potential was ignored because the model domain is relatively small. The longer runs were made to study seasonal and some interannual variability of ice-shelf melt rates, sea-ice evolution, current velocities, and water temperatures. The shorter runs provide output time series that resolve the fundamental diurnal tidal variability.

4. Tidal Signals

Tidal signals are evident in GPS-based ice-shelf height z_{GPS} (Figure 2d) and the northward components of depth-averaged currents (Figure 2g). Harmonic analyses of the different time series were performed using the Matlab software package T_TIDE [*Pawlowicz et al.*, 2002], which is based on *Foreman* [1977]. The analysis first removes the linear trend. The typical record length of ~60 days is too short to explicitly resolve all major tidal constituents; therefore, we estimated the P_1 and K_2 tidal components using inference from K_1 and S_2, respectively, with amplitude-ratio and phase-offset parameters obtained from the ~238 day record of z_{GPS} at M-2 (Table 4). We also used T_TIDE to predict the total tidal signal for the observation time period.

4.1. Ice Surface Elevation

The typical amplitude of tidal elevation variability is ~0.5–1 m (Figure 2d). Tides account for most of the variance (~81% at M-1 and ~95% at M-2) (Table 5) in $z_{GPS}(t)$ after correcting for the IBE (see section 2) and removing the remaining linear trend by T_TIDE. The dominant tidal constituents under RIS are the K_1 principal lunisolar diurnal (period 23.93 h), the O_1 principal lunar diurnal (25.82 h), and the P_1 principal solar diurnal (24.07 h). The diurnal Q_1 (26.87 h) and the major semidiurnal constituents M_2 (12.42 h) and S_2 (12.00 h) are also statistically significant, but their contribution to total tidal variance is small. A strong ~2 week modulation of z_{GPS} is apparent (Figure 2d), caused by superposition of the K_1, O_1, and P_1 constituents.

Table 5. Amplitude (cm) and Phase (Degrees Relative to Greenwich) for the Six Primary Tidal Constituents Based on GPS Measurements Made During the M-1 and M-2 Mooring Deployments[a]

	Amp (cm)		Phase (°)	
Constant	M-1	M-2	M-1	M-2
K_1	22.8 ± 1.7	23.4 ± 1.6	197.2 ± 4.3	198.3 ± 3.9
O_1	20.6 ± 1.7	22.3 ± 1.4	185.2 ± 4.6	184.6 ± 4.9
P_1	7.4 ± 1.5	7.6 ± 1.5	193.5 ± 13.2	194.5 ± 11.6
Q_1	4.2 ± 1.7	4.3 ± 1.6	190.6 ± 23.0	181.3 ± 23.8
M_2	3.4 ± 0.5	3.4 ± 0.4	9.9 ± 9.3	5.1 ± 6.4
S_2	3.6 ± 0.6	3.5 ± 0.4	289.9 ± 9.1	304.9 ± 6.4
	Var (cm^2)	Var (cm^2)		
Total variance	810	860		
Tidal variance	660	800		
Tidal variance (%)	81.3	93.5		

[a]The lower three rows show for each mooring site: (1) the variance of the basic signal; (2) the tidal signal variance; and (3) the percent variance explained by the tides. The mean and trend were removed before the harmonic analysis, and only constituents with signal-to-noise ratios ≥2 were included. The M-1 and M-2 trends had slopes of −0.098 and −0.091 cm h^{-1}, respectively.

4.2. Depth-Averaged Currents

Tides account for about half of the variance in the depth-averaged

Table 6. ANDRILL Depth-Averaged M-1 and M-2 Tidal Ellipse Parameters and 95% Confidence Limits for the Six Primary Constituents[a]

	Major (cm s^{-1})		Minor (cm s^{-1})		Inclination (°)		Phase (°)	
Const.	M-1	M-2	M-1	M-2	M-1	M-2	M-1	M-2
K_1	5.6 ± 0.2	4.9 ± 0.4	0.5 ± 0.3	0.2 ± 0.3	96.3 ± 3.2	93.2 ± 3.9	302.3 ± 2.4	299.0 ± 5.0
O_1	4.0 ± 0.2	3.9 ± 0.4	−0.3 ± 0.3	−0.3 ± 0.3	96.8 ± 4.4	96.6 ± 4.5	274.9 ± 3.6	270.9 ± 6.3
P_1	1.8 ± 0.2	1.6 ± 0.4	0.2 ± 0.3	0.1 ± 0.3	96.3 ± 10.3	93.2 ± 11.0	298.5 ± 6.5	295.2 ± 14.5
Q_1	0.7 ± 0.2	0.9 ± 0.4	0.1 ± 0.3	−0.4 ± 0.3	104.6 ± 25.7	82.1 ± 35.5	269.5 ± 20.6	271.1 ± 43.0
M_2	0.8 ± 0.1	0.7 ± 0.1	−0.2 ± 0.1	−0.2 ± 0.1	96.0 ± 9.7	99.6 ± 10.9	310.1 ± 9.8	302.4 ± 8.3
S_2	1.2 ± 0.1	0.9 ± 0.1	0.0 ± 0.1	−0.0 ± 0.1	98.4 ± 6.0	96.6 ± 7.7	256.9 ± 7.1	253.9 ± 5.8

[a]Inclination angle is measured counterclockwise from east. Phase is given in degrees relative to Greenwich.

current velocities at both moorings (Table 6). The total tidal signal had typical speeds of ∼0.1 m s^{-1}. The major axes (U_{maj}) of tidal current components at both M-1 and M-2 were aligned very close to north-south (Figure 4), roughly normal to the ice-shelf edge (Figure 1). In most cases, the minor axis was not statistically different from zero; therefore, current-vector rotation direction cannot be determined. As with z_{GPS}, tidal currents experience a strong ∼2 week spring-neap modulation (Figure 2g). An expanded list of the ellipse parameters per individual instrument can be found in Tables S3 and S4 in supporting information.

4.3. Hydrographic Time Series

We also performed tidal analyses on the moored salinity, temperature, and density data for individual sensors. Tides made only a small (1–16%) contribution to the variance of hydrographic signals at M-1; they did not contribute significantly at M-2. While there were a few tidal constituents that had significant signal-to-noise ratios at a single depth, these constituents did not extend over depth, indicating there was not a significant coherent internal tidal signal at the mooring sites.

4.4. CATS2008 Barotropic Tide Model

Our tidal analyses of measured elevations and depth-averaged currents were compared with results from the CATS2008 tide model. The tidal elevation and current ellipse parameters derived from our data sets agree with CATS2008. The results are detailed in Tables S1 and S2 in supporting information.

5. Subtidal Variability

5.1. Wind

Winds measured at the Laurie II AWS site were generally toward the northeast, with a few weak reversals toward the west and south (Figure 5). The mean wind during the deployment analysis period was relatively weak, 3.9 m s^{-1} oriented toward 24°N; the strongest winds were >15 m s^{-1}, oriented toward the northeast. The winds were dominated by synoptic-scale events, with kinetic energy concentrated in a clear peak between 0.2 and 0.4 cpd (periods 2.5–5 days) and a smaller peak near 0.1 cpd. There was no evidence of systematic diurnal winds.

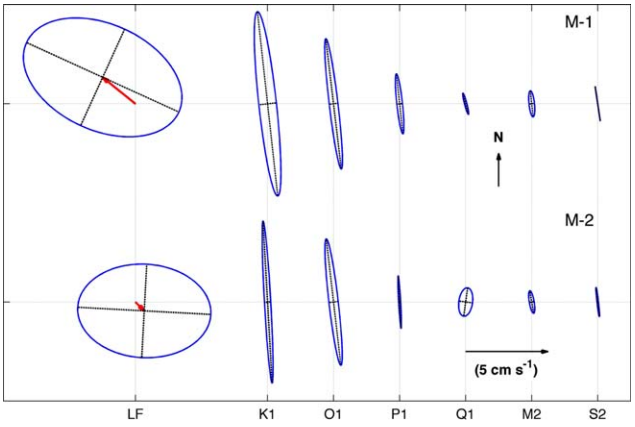

Figure 4. Mean (red vectors) and principal axes of the low-frequency depth-averaged currents shown in first column (LF). Tidal ellipses of depth-averaged currents shown in the six columns to the right. M-1 results in upper row, M-2 results in lower row. K1, O1, and P1 constituents overshadow the Q1, M2, and S2 constituents. The tidal flow is mostly in the North-South direction, perpendicular to the ice-shelf edge. Most minor axes are not statistically significant; therefore, rotation direction is not shown.

To examine the wind variability, we decomposed the wind time series into its two principal components [*Fofonoff*, 1969]. The percent variance for the two components was 79.5% and 20.5%, with the major axis oriented toward ∼35°N, as

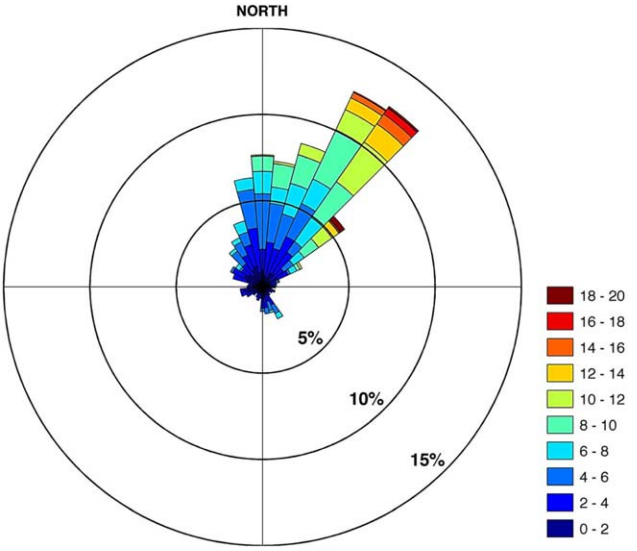

Figure 5. Polar histogram of the hourly averaged AWS wind vectors (U_w, V_w). The histogram has 10° wind direction bins and 2 m s^{-1} wind speed bins, indicated by the color bar to the right. The cumulative arcs indicate the percentage of the time the winds were in that direction and the colored bins the contributions for each wind interval.

expected from the wind rose in Figure 5. Linear regression between the major wind component and air temperature showed a trend of colder air with larger wind speed toward the northeast. The correlation is weak, correlation coefficient, $r = -0.30$, but significant at the 95% confidence level.

5.2. Currents

An Empirical Orthogonal Function (EOF) analysis [*Obukhov*, 1947; *Lorenz*, 1956; *Davis*, 1976] of the current velocity data for each instrument, after filtering out the tides, showed that the subtidal variability was essentially barotropic at each mooring. Each velocity time series was first rotated into a coordinate system aligned along the principal component of the depth-averaged velocity, so that the velocities along each axis are statistically independent. The major axes (Figure 4, first column) were oriented toward 115°N and 89°N at M-1 and M-2, respectively, roughly parallel to the ice front. The two components of the velocity at the five depths were then used to construct a 10 × 10 covariance matrix. The first two EOF modes of the velocity variability at each mooring contained ~70% and ~30%, respectively, of the total variance, i.e., these two leading modes explained almost the entire signal. The first EOF represented a nearly constant velocity along the major axis of the depth-averaged current and the second represented a barotropic current oriented along the minor axis. The ratio of the EOF variances, as expected, is consistent with the ratio of the variances of the depth-averaged currents aligned parallel and perpendicular to the major axis.

5.3. Temperature and Salinity

Data from the four Microcats on M-1 and five on M-2 are shown in Figure 6 as time series of temperature and salinity anomalies from their time-averaged values (Table 7). Salinities at the shallowest instruments on both moorings decrease over the deployment, which might have been caused by an increase in local basal melting and/or changes in fresh-water advection pathways. The coldest temperature at the shallowest instrument, −2.03°C, was slightly above the local in situ freezing point, $T_f(S,P) = -2.06$°C, and most of the record was significantly warmer than $T_f(S,P)$, which suggests that there was significant vertical mixing and/or advection bringing warmer water into the mixed layer below the ice shelf. There is no evidence of freshening at the deeper instruments. From Figure 6 and an EOF analysis of the time series, the temperature variations at the upper two instruments on M-1 are correlated. Similarly, the salinity for the second and third instruments on M-1 are correlated, suggesting that boluses of fresher water passed by the mooring. There are no other significant correlations between the temperature and/or salinity at the other depths on M-1 or for any depths on M-2. While the correlations for the upper sensors on M-1 are statistically significant, it is hard to construct a simple description that consistently links the observed correlation of temperature with the observed boluses seen in the salinity time series. Density (not shown) is almost completely determined by salinity so that time series of density are proportional to salinity.

5.4. Ice Surface Elevation

The GPS elevation record at M-2 ($z_{GPS}(t)$), after correcting for the inverse barometer effect (IBE; see section 2) and removing tides (section 4.1), has a linear least-squares trend of $dz_{GPS}/dt = -0.22$ m a^{-1} for the ~2 month period of the mooring deployment. This negative trend in z_{GPS} represents the hydrostatically compensated response of the ice-shelf surface thinning by basal melting, depression of the ice shelf by surface

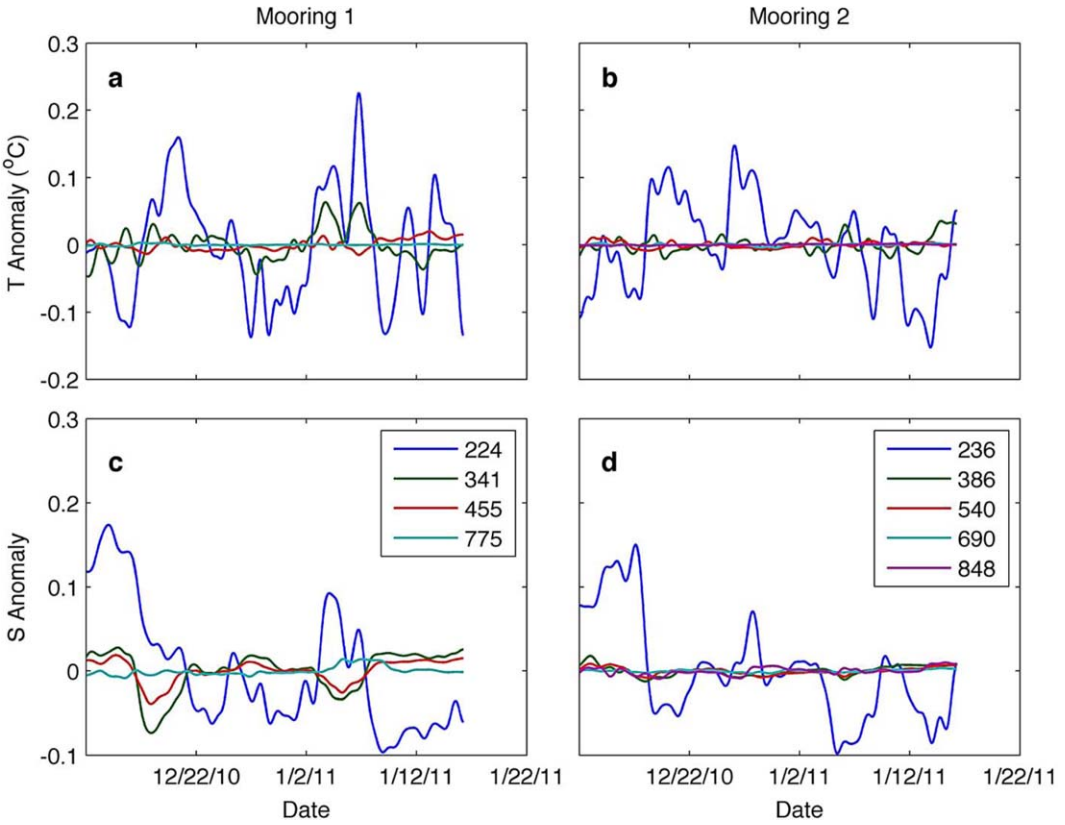

Figure 6. Time series of temperature and salinity anomalies. (a) M-1 temperature, (c) M-1 salinity, (b) M-2 temperature, and (d) M-2 salinity. Instrument depths listed in lower plots.

mass accumulation, divergence of lateral ice flow [e.g., *Padman et al*., 2012], and/or firn compaction (densification of the upper snow layers) [*Ligtenberg et al*., 2011].

6. Basal Melt Rates

6.1. Estimates From Mooring Records

We estimated the time series of basal melt rate $w_b(t)$ by equating the divergence of the vertical flux of sensible heat at the ice base (ΔQ_S) with the latent heat (Q_L) associated with melting ice [*Holland and Jenkins*, 1999]. The value of ΔQ_S was obtained from the difference between the upward flux of ocean sensible heat (Q_O) and the conductive heat flux through the ice (Q_I), the latter depending on the temperature gradient in the ice at the base of the ice shelf. This gradient, in turn, depends on w_b. Following *Holland and Jenkins* [1999, equation (25)], for an ice shelf 250 m thick with long-term-averaged top surface temperature $\sim -25°C$ (the annual mean for the entire RIS based on the ERA Interim atmospheric reanalysis model [*Dee et al*., 2011]), Q_I is $\sim 0.2 Q_O$ for the expected range of basal melt rates near the ice front ($\sim$1–5 m a^{-1}: *Horgan et al*. [2011]).

Table 7. Record Mean and Standard Deviation of Temperature and Salinity Measured With the Microcats Deployed at M-1 and M-2

	Depth (m)	T Mean (°C)	T std (°C)	S Mean	S std
M-1.1	224	−1.890	0.082	34.381	0.073
M-1.2	341	−1.911	0.023	34.612	0.025
M-1.3	445	−1.912	0.008	34.669	0.013
M-1.4	775	−1.887	0.001	34.735	0.005
M-2.1	236	−1.869	0.066	34.393	0.060
M-2.2	386	−1.914	0.012	34.646	0.006
M-2.3	540	−1.899	0.005	34.669	0.004
M-2.4	690	−1.892	0.002	34.719	0.001
M-2.5	848	−1.884	0.001	34.743	0.004

We first estimated Q_O at the ice base under RIS due to turbulence associated with currents, using the turbulent flux parameterization of *McPhee et al*. [1999], their equation (1):

$$Q_O = \rho_w C_p C_H u_* \Delta T, \quad (1)$$

where ρ_w is water density (kg m^{-3}), C_P

Table 8. Estimated Ocean Heat Flux (Q_O) and Melt Rate (w_b) at the ANDRILL Mooring Sites Derived From Equations (1) to (3), Section 6.1

	Q_O (W m^{-2})		Q_O From Tides (W m^{-2})		w_b (m a^{-1})		w_b From Tides (m a^{-1})	
	M-1	M-2	M-1	M-2	M-1	M-2	M-1	M-2
Mean	18	17	8	10	1.3	1.2	0.6	0.7
Standard error	1.1	9.1	3.9	2.1	0.4	0.6	0.3	0.2
N degrees of freedom	31	19	22	26	31	19	22	26

($\sim$4000 J kg^{-1} °C^{-1}) is specific heat for cold salt water with $S = 32$, C_H is the Stanton number (taken as 0.005 [*McPhee et al*., 1999]), u_* (m s^{-1}) is the friction velocity, and ΔT(°C) is the difference between the in situ temperature measured with the closest Microcat to the ice base and the pressure-dependent freezing temperature of seawater, $T_f(S, P)$. *McPhee et al*. [1999] measured u_* directly with microscale turbulence sensors below sea ice, while *Stanton et al*. [2013] obtained similar direct measurements of u_* below Pine Island Glacier's ice shelf. However, in the absence of microstructure measurements resolving the turbulence, we estimated u_* from the quadratic stress formulation:

$$u_* = C_D^{1/2}|\mathbf{u}|, \tag{2}$$

where C_D is the drag coefficient and $|\mathbf{u}|$ is current speed (m s^{-1}) from the Aquadopp current meter closest to the ice base (7.4 m below the ice at M-1 and 8.0 m below the ice at M-2). The correct value of C_D for this environment is not known: based on sea-ice studies, a likely range is $\sim$0.001–0.006 [*Harder and Fischer*, 1999]. We use a midrange value of $C_D = 0.003$ in our numerical models, which is close to the value inferred from the ratio of mean current and u_* in *Stanton et al*. [2013, Figure 4]. However, uncertainty in C_D is a major source of uncertainty in heat fluxes based on equation (1). The mean upward ocean sensible heat flux was then estimated as the time-average of $Q_O(t)$ using the time series of $u_*(t)$ and $\Delta T(t)$ in equation (1). Given that estimated Q_I is $\sim 0.2Q_O$, the net heat available at the ice base is $\Delta Q_S \approx 0.8Q_O$.

The latent heat of ice melt is:

$$Q_L = -\rho_i L_F w_b, \tag{3}$$

where L_F is the latent heat of fusion ($=3.34 \times 10^5$ J kg^{-1} [*Holland and Jenkins*, 1999]), and $\rho_i = 918$ kg m^{-3} is the density of ice. Equating $0.8Q_O$ with Q_L gives w_b in terms of ΔT and u_*. The time-averaged values of Q_O and w_b estimated in this manner from the mooring data, with C_D in the range 0.001–0.006, are $\sim 17 \pm 7$ W m^{-2} and $\sim 1.2 \pm 0.5$ m yr^{-1}, similar for both M-1 and M-2 (Table 8).

The time series of $|\mathbf{u}|$ and ΔT for M-1 (Figures 7a and 7b) show large variability on tidal and subtidal timescales. Combining these through equations (1–3), and using a midrange value of $C_D = 0.003$, the estimated instantaneous values of w_b varied from near-zero to $\sim$7 m a^{-1} during the mooring deployment (Figure 7c). The maximum value is about 5 times larger than the time-averaged value. We also estimated the sensible heat flux attributable solely to tides using the time series of $\mathbf{u}_T(t)$ predicted from the tidal constituents (see section 4.2) to provide an estimate of u_* from equation (2) and the tidal contribution to w_b (Figure 7d). About half of the mean ocean heat flux (for $C_D = 0.003$, $\sim$8 W m^{-2} at M-1; $\sim$10 W m^{-2} at M-2) and its consequent melt rate ($\sim$0.6 m a^{-1} at M-1; $\sim$0.7 m a^{-1} at M-2) can be attributed to the presence of tidal currents (Table 8). The value of w_b varied roughly fortnightly, with higher values during spring tides and lower values during neap tides (Figures 7c and 7d). Deviation from a pure spring-neap cycle is explained by subtidal variability of upper ocean temperature (Figure 7b).

6.2. Modeled Basal Melt Rates

Maps of the time-averaged values of $w_b(\mathbf{x})$ evaluated from the 2 year ROMS runs (section 3) without and with tides (Figure 8), show large modeled melt rates are along the western RIS grounding line south of Ross Island, under the southeastern RIS (Siple Coast) and along the ice front. The integrated ice volume loss rate from RIS, for the simulation without tides, is $\sim$117 km^3 a^{-1} (an average melt rate of $w_b \sim 0.25$ m a^{-1}) averaged over 2 years. Adding tidal forcing increases these rates by $\sim$25–30%, to $\sim$150 km^3 a^{-1} and 0.32 m a^{-1}. The largest

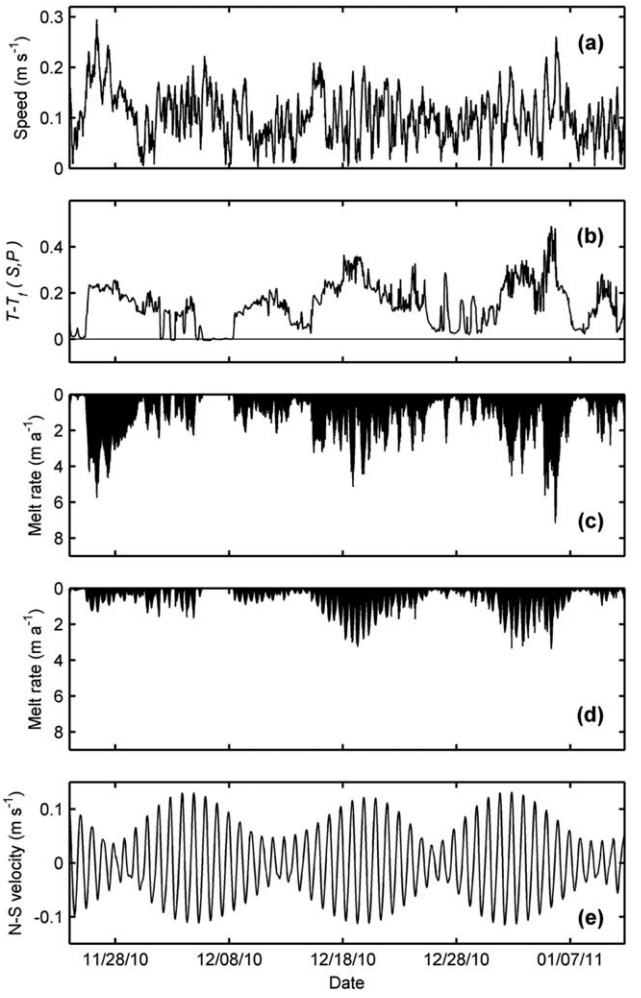

Figure 7. M-1 melt rate. (a) Current speed just below ice base. (b) Temperature T relative to in situ freezing point $T_f(S,P)$ just below ice base. (c) Melt rate w_b estimated using raw current speed, T-$T_f(S,P)$, and equations (1–3). (d) Same as Figure 7c, but using tidal velocities only. (e) North–South tidal velocity component. The beat phenomenon is due to the fortnightly modulation (spring-neap cycle) from superposition of major diurnal tidal constituents.

time-averaged modeled melt rates are found in a narrow zone along the ice front. We refer to this region as the ice-shelf frontal zone (ISFZ), and formally define it as the area of ice shelf within 30 km of the ice front. The area of the ISFZ is ~33,000 km^2, about 7% of the entire area of RIS. The mean values of w_b for this region are ~1.3 and ~1.7 m a^{-1} for the no-tides and tide-forced simulations, respectively. These values are ~5 times larger than the RIS-averaged values, so that the net contribution of modeled melting from the ISFZ is ~35% of the total from the complete RIS. Maximum values in the simulation with tides are ~4.5 m a^{-1} compared with ~2–3 m a^{-1} in the no-tides run.

The model simulations are not directly comparable to the observations for several reasons. First, the time periods are different. Second, the model lateral grid spacing of 5 km does not adequately resolve the known large variations of ocean processes and melting rates across the ISFZ. Third, the use of terrain-following coordinates requires that the ice draft is smoothed, reducing the abruptness of the change in water column thickness at the true ice front [see *Mueller et al*., 2012, supporting information]. Finally, the ice front location in our model is several kilometers south of its position during the measurement program described herein; the RIS ice front in this region advances at about 1 km a^{-1} [*Rignot et al*., 2011]. However, in order to compare modeled variability of melt rates with the results from the analyses of measurements, we extracted output at three "virtual" mooring locations (see Figure 8): two (VM-1 and VM-2) correspond to the distances of the M-1 and M-2 mooring sites south of the ice front, and the third (named VM-3) is at the first grid node located just south of the ice front.

Modeled values of w_b at each virtual mooring, averaged over the full length (~2 years) of each run (Table 9), show that adding tides to the forcing increases the mean melt rate at each site by ~50%, slightly more than for the average over the entire ISFZ. The mean values of w_b at VM-1 and VM-2, in the tide-forced runs, are close to the values estimated from the M-1 and M-2 mooring data (see section 6.1) when using the same value of C_D (0.003) used in the models. Modeled values of w_b are about a factor of 3–4 higher at VM-3 (very close to the ice front) than further south at VM-1. However, modeled ice draft at this location is ~80 m, which is much less than the real value of 219 m, a consequence of grid smoothing required for numerical stability in ROMS. The shallower model ice draft provides easier access to the sub-ice-shelf cavity for seasonally warmed near-surface waters in the Ross Polynya; see *Mahoney et al*. [2011], their Figure 4.

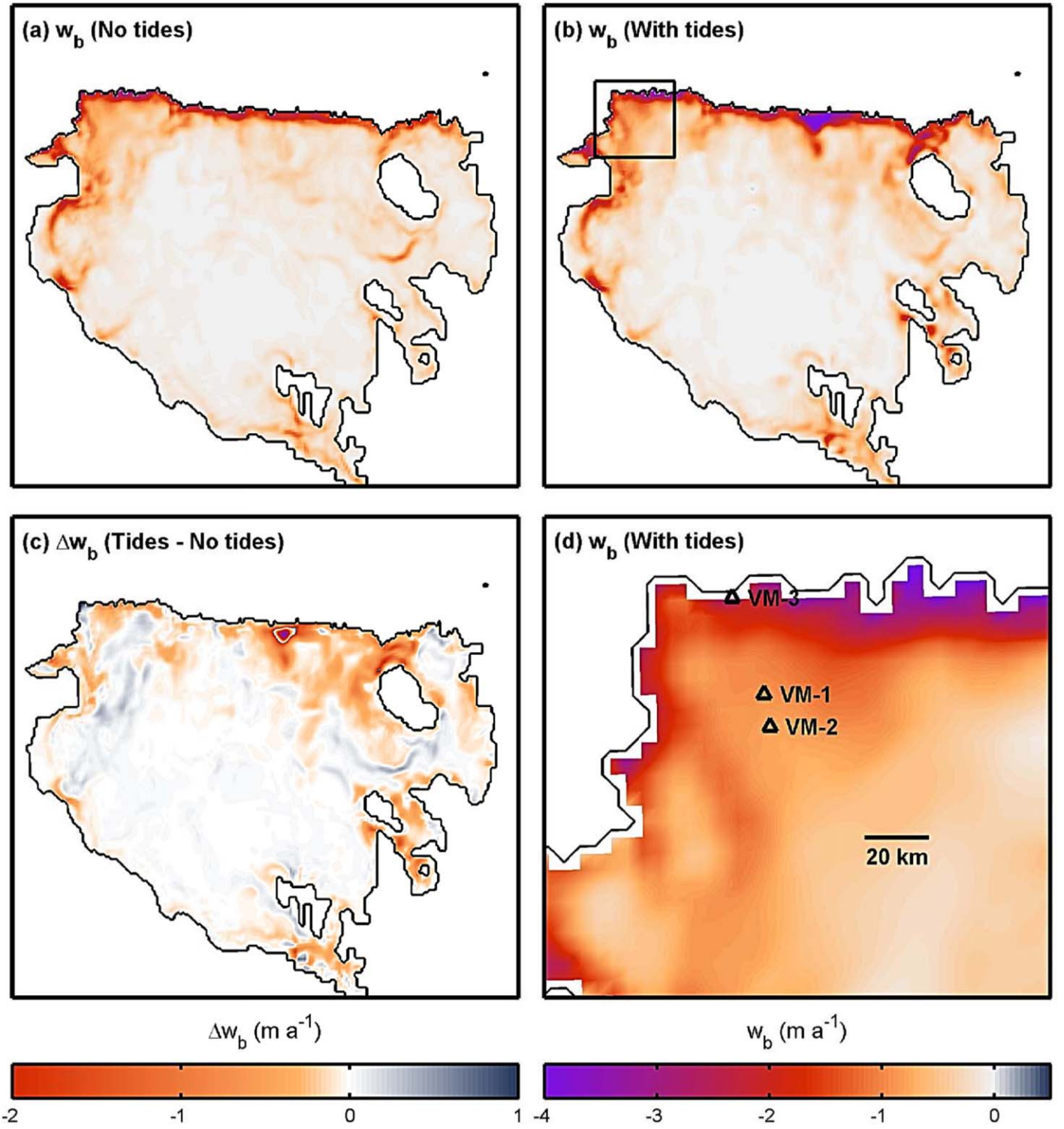

Figure 8. (a) Modeled time-averaged basal melt rate w_b (m a^{-1}: color scale at bottom right) from ROMS run for 2 years, with atmospheric forcing but no tidal forcing. Values of $w_b < 0$ imply ice-shelf mass loss. (b) Same as Figure 8a, but for model with tide forcing included. (c) Difference in basal melt rate between runs with and without tides. Color scale is at bottom left. Negative values imply more basal melting in run with tides. (d) Basal melt rate for region shown by black rectangle in Figure 8b. Locations of virtual moorings (VM-1, VM-2, and VM-3) are indicated: VM-1 and VM-2 approximate locations of real moorings M-1 and M-2 relative to the ice edge; VM-3 is the closest model point to the ice front.

Table 9. Modeled Melt Rates at the Three Virtual Mooring Stations (VM-1 and VM-2 Close to M-1 and M-2, Respectively, and VM-3 Very Close to the Ice Edge)

	Average Melt Rate (m yr^{-1})		Max. Melt Rate (m yr^{-1})	
	No Tides	With Tides	No Tides	With Tides
VM-1	0.89	1.31	2.70	4.22
VM-2	0.84	1.20	2.63	4.91
VM-3	3.20	4.70	13.46	21.95

The 2 year time series (September 2003 to September 2005) of modeled $w_b(t)$, 5 day averaged barotropic ocean current component normal to the ice front $u_n(t)$, and potential temperature $\theta(t,z)$ at VM-1 and VM-3 show pronounced quasi-annual and some interannual variability (Figure 9). The onset of thermal stratification under the ice shelf occurs in December or early January and the water column returns to its winter cold state between early May and late July. The highest modeled values of θ, $\sim -1.2^{\circ}$C, are higher than the expected maximum of $\sim -1.5^{\circ}$C just seaward of the ice front from hydrographic compilations [*Orsi and Wiederwohl*, 2009] and mooring data [*Pillsbury and Jacobs*, 1985], but generally consistent with data from a mooring beneath sea ice in nearby McMurdo Sound [*Mahoney et al*., 2011, Figure 4]. Through other model runs, not described here, we have found that the modeled temperature of subsurface waters along the RIS ice front is sensitive to the surface radiation budget in austral summer (in turn, dependent on sea ice concentration, thickness and snow cover), and choice of wind forcing model as a control on southward advection of Modified Circumpolar Deep Water (MCDW). We will explore this sensitivity in more detail in a future study.

The 6 month simulations with 4 h output cover the onset and decay of the subice-shelf thermal maximum in austral summer 2004–2005 (Figure 10). There is large variability of modeled w_b at short timescales, including the period of the fundamental (primarily diurnal) tides, the ~2-week modulation of the spring/neap cycles, and other subtidal fluctuations. In our simulations, the reduction in stratification in late March is accompanied by an increase in the variance of subtidal currents (Figure 10). This is true for simulations without and with tidal forcing.

7. Discussion

The linear trend in ice-shelf surface elevation from the IBE-corrected GPS record ($dz_{GPS}/dt \approx -0.22$ m a^{-1}: section 5.4) provides a coarse check on our estimates of w_b. Change in elevation reflects the hydrostatic response to basal melting, ice mass divergence (ice "stretching"), and changes in the density of compacted snow ("firn") under the support for the GPS; see *Padman et al*. [2012] for a discussion of these terms applied to Wilkins Ice Shelf. We expect the elevation trends due to ice divergence at the ice front to be negative, and the trend due to firn compaction should also be negative during summer months; therefore, the GPS estimate is an upper limit on thinning associated solely with basal melting. If we interpret dz_{GPS}/dt solely as the response to basal melting (assuming hydrostatic balance), $w_b = (\rho_w - \rho_i)(dz_{GPS}/dt)/\rho_w \approx 2.1$ m a^{-1}, averaged over the ~2 month period. After taking into account the other thinning terms, we regard our thermodynamic estimates of w_b as being generally consistent with the GPS record.

These local values of w_b are an order of magnitude greater than previously reported values that have been averaged over the entire RIS; the latter are in the range ~0.1–0.3 m a^{-1} (Table 10). Our higher values in the ISFZ are, however, consistent with the near-ice-front amplification of basal melting seen in previously published numerical models [*Holland et al*., 2003; *Dinniman et al*., 2007], analyses of satellite laser altimetry [*Horgan et al*., 2011], and measurements under the nearby McMurdo Ice Shelf [*Stern et al*., 2013].

The M-1 and M-2 mooring time series are too short to identify seasonal changes in w_b estimated from equations (1) to (3) applied to the measurements of T and $|\mathbf{u}|$ close to the ice base (Figure 7c). However, there is a large annual cycle of modeled seasonal variability of w_b (Figure 9). The phasing of the annual cycle depends on proximity to the ice front, and whether tidal forcing is included in the simulations. At virtual mooring VM-3, close to the ice front, w_b is largest in austral summer and consistently weaker in winter. Adding tides increases the contrast between winter and summer (compare Figures 9d and 9j). At VM-1, several

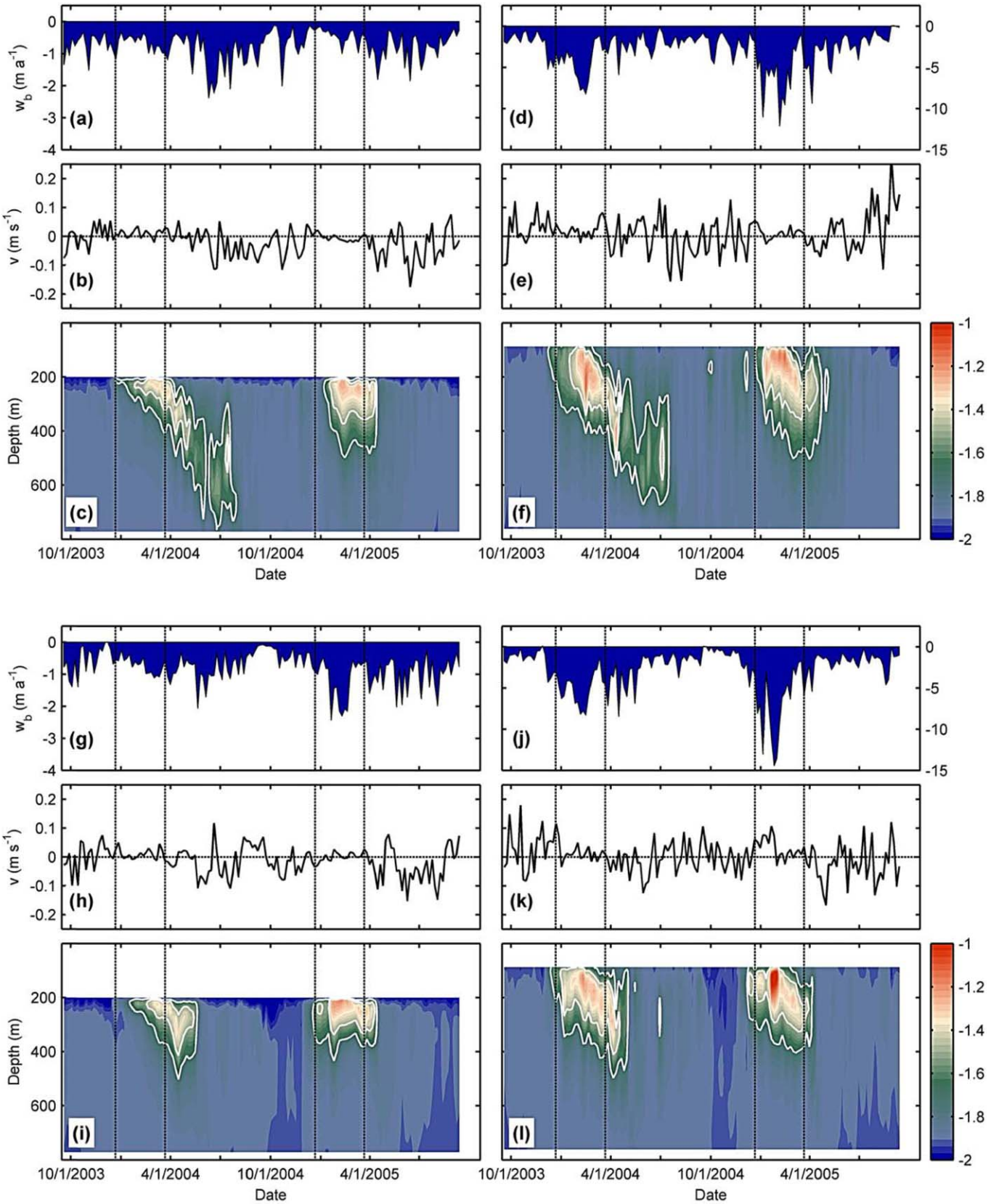

Figure 9. (a–c) Basal melt rate w_b (m a^{-1}), northward component of depth-averaged current and ocean potential temperature (θ) at virtual mooring VM-1 (see Figure 8 for location) for ROMS simulation for 2 years at 5 day averaged output time step with atmospheric but no tidal forcing. (d–f) Same as Figures 9a–9c but for VM-3 close to the ice front. (g–i) Same as Figures 9a–9c but with tidal forcing included. (j–l) Same as Figures 9d–9f but with tidal forcing included. In Figures 9c, 9f, 9i, and 9l, white contours indicate $\theta = -1.7°$C and $-1.5°$C. Note different *y* axes on basal melt rate plots (a), (d), (g), and (j). Vertical-dashed lines indicate start and end of summer, defined as 21 December (summer solstice) to 21 March (fall equinox).

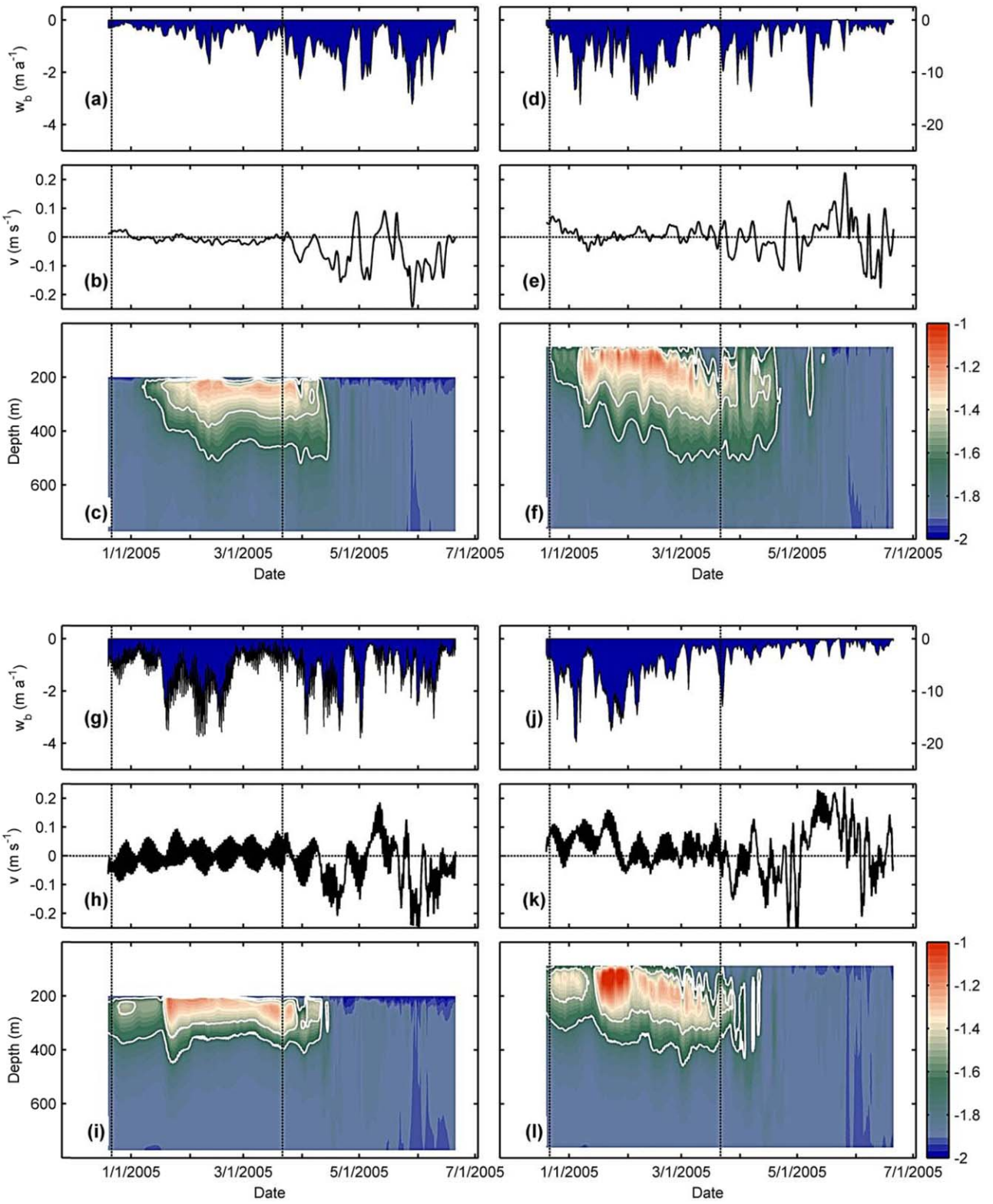

Figure 10. (a–c) Basal melt rate w_b (m a^{-1}), northward component of depth-averaged current and ocean potential temperature (θ) at virtual mooring VM-1 (see Figure 8 for location) for ROMS simulation for 6 months at 4 h averaged output time step with atmospheric but no tidal forcing. (d–f) Same as Figures 10a–10c but for VM-3 close to the ice front. (g–i) Same as Figures 10a–10c but with tidal forcing included. (j–l) Same as Figures 10d–10f but with tidal forcing included. In Figures 10c, 10f, 10i, and 10l, white contours indicate $\theta = -1.7°C$ and $-1.5°C$. Note different *y* axes on basal melt rate in Figures 10a, 10d, 10g, and 10j. Vertical-dashed lines indicate start and end of summer, defined as 21 December (summer solstice) to 21 March (fall equinox).

Table 10. Melt Rates, Averaged Over the Entire Ross Ice Shelf, Obtained in Our Simulations and Other Studies

Average Melt Rate (m a^{-1})	Source	Details
0.11 ± 0.3	*Shabtaie and Bentley* [1987]	Melting rates estimated from radar soundings (1984–1985) and RIGGS ice velocities Measurements exclude the 100 km closest to the ice front
0.25	*Assmann et al.* [2003]	Circumpolar numerical model Only takes into account 80% area Excludes ice-shelf edge, and without tidal forcing
0.082	*Holland et al.* [2003]	Modified Miami Isopycnic Coordinate ocean model Without tidal forcing
$0.13 - 0.15$	*Dinniman et al.* [2007]	ROMS model Without tidal forcing
0.15	*Dinniman et al.* [2011]	ROMS model Without tidal forcing
0.10 ± 0.07	*Rignot et al.* [2013]	Derived from satellite data, and models for surface mass balance and firn densification
0.15 ± 0.06	*Depoorter et al.* [2013a, 2013b]	Derived from satellite data, and models for surface mass balance and firn densification
0.11 ± 0.14	*G. Moholdt et al.* (Basal mass budget of Ross and Filchner-Ronne ice shelves, Antarctica, derived from Lagrangian analysis of ICESat altimetry, submitted to *Journal of Geophysical Research Earth Surfaces*, 2014)	Derived from satellite data, and models for surface mass balance and firn densification
	This study	ROMS model
0.25		Without tidal forcing
0.32		With tidal forcing

kilometers south of the modeled ice front, the highest values of w_b occur in winter in simulations without tides, and inconsistently throughout the year in simulations with tidal forcing (compare Figures 9a and 9g, and Figures 10a and 10g).

The variability of basal melting will impact the contribution of the freshwater fluxes to other processes in the Ross Sea including the potential for ice-shelf meltwater to affect sea-ice growth and suppress the upward flux of surface heat and nutrients to the upper ocean.

Other studies have also reported seasonality in basal melt rates. *Holland et al*. [2003] predicted a melting rate maximum at the end of winter when values were averaged over the full RIS area. *Assmann et al*. [2003] calculated two maxima for basal melting under RIS, one in March and one in August. Those authors attributed the March maximum to high water temperatures and the August maximum to strong sub-ice-shelf circulation. On longer timescales, interannual variability in our ROMS results (Figure 9) could be a consequence of differences in sea-ice cover [*Horgan et al*., 2011] and wind forcing.

Time series of w_b, estimated from our mooring data using equations (1–3) (Figure 7), and from our ROMS models (Figures 9 and 10), also show significant variability at timescales from days to weeks. We assume that the contribution of subtidal currents to net melting is important, since the instantaneous subtidal currents greatly exceed the magnitude of the mean flows (Figure 4). One component of this variability is associated with ~14 day spring/neap modulation of the tidal currents (Figure 7). However, subtidal variability also occurs in simulations with no tidal forcing (Figures 10a–10f); in that case, time-dependence of $w_b(t)$ arises from a combination of subtidal currents and variations in the availability of ocean heat from the relatively warm water underlying the ISFZ in austral summer. In our simulations, the variance of subtidal ocean currents changes quite rapidly, from negligible when the warm water is present under the ISFZ in summer to a maximum when the ocean cools back to near the surface freezing point of $\sim -1.9^{\circ}$C in late March or April. The opposite transition is observed by the moorings, with a rapid reduction in subtidal current variance in late December (Figures 2e and 2f). In that case, there is no clear association with measured hydrographic changes at the mooring sites. Based on the difference in seasonal phasing of modeled melt rate near the ice front and further south, we attribute the change in the measured velocities at the moorings to dynamic changes closer to the ice front and in the Ross Polynya, where stratification is known to vary greatly from winter to summer [*Pillsbury and Jacobs*, 1985].

We do not yet understand the processes causing subtidal currents. From comparisons of data from the moorings and the AWS, these currents are not directly correlated with local winds (section 5). Instead, we

postulate that subtidal currents are eddies, frontal instabilities or vorticity waves [*MacAyeal*, 1985] whose properties are modulated by the density contrast between the water in the Ross Polynya and the water under the ISFZ. Given the apparent importance of these subtidal currents to mean basal melting in the ISFZ, developing a better understanding of their generation mechanisms is an important next step in understanding ice-shelf/ocean interactions.

Tides play a clear role in modulating w_b derived from mooring time series. Modulation occurs at both the fundamental tidal frequency (diurnal along the RIS front) and at the spring/neap timescale of ~14 days. Adding tidal forcing to our numerical model increased the basal melt rate near the ice front and northeastern RIS by about 30% (Table 9 and Figures 8 and 10). This result is consistent with observations of Filchner-Ronne Ice Shelf (FRIS) by *Joughin and Padman* [2003], who recognized that maps of spatial melt distribution for FRIS were qualitatively similar to maps of mean tidal speeds, showing higher melt rates in locations (including the ISFZ) with stronger velocity magnitudes. *Makinson et al*. [2011], in their model of FRIS, found that adding tides to their model tripled the total kinetic energy under the FRIS, intensifying water mass exchange through the ice front and more than doubling melt rates near the ice edge. *Mueller et al*. [2012] reported a similar response to tides in their model of Larsen C Ice Shelf.

8. Conclusions

We used data from two moorings, deployed through Ross Ice Shelf (RIS) about 6 and 16 km south of the ice front east of Ross Island, to identify processes contributing to basal melting near the ice front. The moorings recorded time series of temperature, salinity, and currents for about 2 months beginning late November 2010. Coincident measurements of local atmospheric state were obtained from a nearby automatic weather station, while GPS measurements at the mooring sites provided high-resolution time series of ice-shelf surface elevation. We augmented analyses of these data with numerical simulations using a 3-D ocean model coupled to a sea-ice model and a thermodynamically active ice shelf. These models were forced with reanalysis atmospheric conditions and, for some runs, tidal forcing at the models' open-ocean boundaries.

The mean basal melt rate w_b (~1.2 ± 0.5 m a^{-1}) at the moorings is 5–10 times higher than for the average over the entire RIS, with the ice-shelf frontal zone (ISFZ: defined as the region of ice shelf within 30 km of the ice front) contributing about 35% of total RIS basal mass loss even though the ISFZ is only ~7% of the RIS area. Basal melt rate varies on multiple timescales including interannual, annual (season cycle), subtidal (timescales of several days), and at the frequency of the fundamental tidal currents, which are primarily diurnal. Seasonal variability is associated with the availability of relatively warm water in the southern Ross Sea, resulting from both increased southward advection of MCDW and a short (~2 month) period of net downward radiative flux into the upper ocean during the summer when the Ross Polynya is free of sea ice. The magnitude of subtidal currents appears to be correlated with changes in conditions along the ice front: based on both measurements and models, we postulate that the variance of subtidal currents is largest when the stratification in the adjacent Ross Polynya is weakest, in winter. Our analyses of mooring data, and comparisons of model runs without and with tidal forcing, suggest that the presence of tidal currents increases w_b by ~30–50% in the ISFZ relative to a no-tides state.

The presence of a narrow zone along the RIS ice front, in which the processes affecting melting rate depend on proximity to seasonally warmer upper-ocean water in the Ross Sea, lead us to hypothesize the following mechanism for accelerated mass loss from RIS. Upper-ocean heat content in the southern Ross Sea in summer may increase through reduced sea-ice cover allowing a longer summer season of net downward heat flux into the upper ocean, and/or an increased southward flux of MCDW associated with changing wind stress. Increased basal melting in the ISFZ would decrease the ice-shelf thickness and allow easier advection of warmer upper-ocean ocean water into the cavity. This process may lead to retreat of the ice front as the thinner ice is more susceptible to calving. Since the elevated melt rate in the ISFZ is related to proximity to the open ocean rather than to geographic location, we hypothesize that this retreat would be self-sustaining provided the large-scale causes of increased southern Ross Sea ocean heat content remain in place. This proposed mechanism for ice loss from RIS is a pathway for retreat of RIS that is not represented in recent analyses and models that focus on the delivery of more CDW/MCDW heat to the deep grounding lines. We emphasize, however, that this hypothesized response depends on several processes that are poorly understood, including the decrease in subtidal variability when the ocean is stratified in

summer, changes in tidal currents as water column thickness and ice-shelf extent changes, and the response of sea ice to freshwater fluxes from the ice shelf.

Improving our confidence in the validity of this mechanism for RIS retreat requires additional data and improved modeling. The apparent strong seasonality of w_b indicates the need for moorings of 1 year or greater duration. Such moorings would provide knowledge of the seasonal variability of ocean heat in the ISFZ, and also better resolution of the modulation of subtidal variance. Our estimates of w_b at the moorings, based on equations (1–3) (section 6.1), are subject to large uncertainties due to dependence on constants derived from studies from under sea ice. A much more accurate measurement of upward ocean sensible heat flux can be obtained from turbulence instruments; see *Stanton et al*. [2013]. Basal melting can be directly measured using phase-sensitive radar [see e.g., *Corr et al*., 2002; *Jenkins et al*., 2006]. These measurements avoid the uncertainties in estimating w_b from changes in ice-shelf surface elevation, which is also affected by lateral divergence of the ice shelf and changes in properties of the ice-shelf firn (the upper layer of less dense snow/ice).

Our present models lack the resolution required to accurately represent the spatial variability of processes close to the ice front. The grid spacing of 5 km is close to the local Rossby radius of deformation, potentially preventing the model from generating the small-scale features responsible for the observed subtidal variability in both stratification and currents. The grid spacing, in our model with terrain-following coordinates, also leads to the need for significant smoothing of ice draft, so that the abrupt change in water column thickness at the ice front cannot be accurately represented. This problem can be mitigated by using a finer grid, either throughout the model domain or by using unstructured-grid finite-volume models rather than our uniform-grid, finite-difference scheme. Our results also indicate sensitivity of basal melting in the ISFZ to ocean state in the Ross Polynya, via the seasonal suppression of subtidal current variance. Models need to accurately represent sea ice and ocean/atmosphere heat, momentum, and moisture fluxes in this complex region that is strongly influenced by the northward flow of cold, dry air off the ice shelf.

We conclude that mass loss from the ISFZ is a significant fraction of net ice loss from RIS, has the potential to vary rapidly if changing large-scale climate modifies the southern Ross Sea upper-ocean heat content, and is sensitive to small-scale processes acting over a wide range of timescales from tidal to interannual. The potential for this mode of climate-induced ice-shelf retreat to occur implies the need for further studies, including longer-term mooring deployments specifically designed to investigate basal melting, and modeling efforts focused on accurate representation of the ISFZ and its interaction with the Ross Polynya.

Acknowledgments

The Woods Hole Oceanographic Institution (WHOI) participation in the ANDRILL Coulman High Program was supported by the National Science Foundation Office of Polar Programs (NSF ANT-0839108) through a subcontract from the University of Nebraska, Lincoln (UNL). This subcontract (UNL 25-0550-0004-004) provided support for R. Limeburner, R. Beardsley, and B. Owens in the planning, field work, and subsequent scientific analysis. I. Arzeno was supported as a 2011 WHOI Summer Student Fellow through the NSF Research Experiences for Undergraduates program (OCE-0649139). L. Padman and S. Springer were supported by NASA grant NNX10AG19G to Earth & Space Research (ESR). M. Williams and C. Stewart were supported by the New Zealand National Institute of Water and Atmosphere (NIWA) core funding under the National Climate Centre, and the Ministry of Business, Innovation, and Employment (Contract CO5X1001). We also wish to acknowledge the following: S. Maas (Victoria University of Wellington) and W. Ostrom (WHOI), for making the field operation successful and safe; S. Fischbein (ANDRILL; UNL) and M. King (U. Tasmania) for providing GPS ice-shelf altitude data collected at M-1 and M-2; C. Laird (Center for Remote Sensing of Ice Sheets, U. Kansas) for providing radar-sensed Ross Ice Shelf thickness near Coulman High; S. Howard (ESR) for help with the ROMS modeling component, with input from the model developer M. Dinniman (Old Dominion University). We greatly appreciate the superb support provided by the ANDRILL Program, the entire Coulman High ice camp community, the NSF Raytheon Polar Services at McMurdo Station, and the Antarctica NZ Scott Base staff. Three anonymous reviewers provided valuable advice that helped us improve this paper. Publication of this paper was funded by the National Science Foundation (OCE-1233598). This is ESR Publication number 151.

References

Agnew, D. C. (1996), SPOTL: Some programs for ocean-tide loading, *SIO Ref. Ser. 96-8*, 35 pp., Scripps Inst. of Oceanogr., La Jolla, Calif.

Agnew, D. C. (1997), NLOADF: A program for computing ocean-tide loading, *J. Geophys. Res.*, *102*, 5109–5110.

Assmann, K., H. Hellmer, and A. Beckmann (2003), Seasonal variation in circulation and water mass distribution on the Ross Sea continental shelf, *Antarct. Sci.*, *15*, 3–11, doi:10.1017/S0954102003001007.

Beardsley, R. C., and L. K. Rosenfeld (1983), Introduction to the CODE-1 moored array and large-scale data report, in *CODE-1: Moored Array and Large-Scale Data Report*, edited by L. K. Rosenfeld, *Woods Hole Oceanogr. Inst. Tech. Rep. WHOI-83-23, CODE Tech. Rep. 21*, pp. 1−16, Woods Hole Oceanogr. Inst., Mass.

Bromwich, D. H., A. J. Monaghan, K. W. Manning, and J. G. Powers (2005), Real-time forecasting for the antarctic: An evaluation of the Antarctic Mesoscale Prediction System (AMPS), *Mon. Weather Rev.*, *133*(3), 579–603, doi:10.1175/MWR-2881.1.

Budgell, W. P. (2005), Numerical simulation of ice-ocean variability in the Barents Sea region: Towards dynamical downscaling, *Ocean Dyn.*, *55*, 370–387, doi:10.1007/s10236-005-0008-3.

Chelton, D. B., and D. B. Enfield (1986), Ocean signals in tide gauge records, *J. Geophys. Res.*, *91*, 9081–9098.

Corr, H. F. J., A. Jenkins, K. W. Nicholls, and C. S. M. Doake (2002), Precise measurement of changes in ice-shelf thickness by phase-sensitive radar to determine basal melt rates, *Geophys. Res. Lett.*, *29*(8), 1232, doi:10.1029/2001GL014618.

Davis, R. E. (1976), Predictability of sea surface temperature and sea level pressure anomalies over the North Pacific Ocean, *J. Phys. Oceanogr.*, *6*, 249–266.

Dee, D. P., et al. (2011), The ERA-Interim reanalysis: Configuration and performance of the data assimilation system, *Q. J. R. Meteorol. Soc.*, *137*(656), 553–597, doi:10.1002/qj.828.

Depoorter, M. A., J. L. Bamber, J. A. Griggs, J. T. M. Lenaerts, S. R. Ligtenberg, M. R. van den Broeke, and G. Moholdt (2013), Calving fluxes and basal melt rates of Antarctic ice shelves, *Nature*, *502*, 89–92, doi:10.1038/nature12567.

Dinniman, M. S., J. M. Klinck, and W. O. Smith Jr. (2007), Influence of sea ice cover and icebergs on circulation and water mass formation in a numerical circulation model of the Ross Sea, Antarctica, *J. Geophys. Res.*, *112*, C11013, doi:10.1029/2006JC004036.

Dinniman, M. S., J. M. Klinck, and W. O. Smith Jr. (2011), A model study of Circumpolar Deep Water on the West Antarctic Peninsula and Ross Sea continental shelves, *Deep Sea Res., Part II*, *58*, 13–16, 1508–1523, doi:10.1016/j.dsr2.2010.11.013.

Dupont, T. K., and R. B. Alley (2005), Assessment of the importance of ice-shelf buttressing to ice-sheet flow, *Geophys. Res. Lett.*, *32*, L04503, doi:10.1029/2004GL022024.

Egbert, G. D., and S. Y. Erofeeva (2002), Efficient inverse modeling of barotropic ocean tides, *J. Atmos. Oceanic Technol.*, *19*(2), 183–204.

Fofonoff, N. P. (1969), Spectral characteristics of internal waves in the ocean, *Deep Sea Res. Oceanogr. Abstr.*, *16*, 59–71.
Foreman, M. G. G. (1977), Manual for tidal heights analysis and prediction, *Pac. Mar. Sci. Rep*. 77-10, Inst. of Ocean Sci., Patricia Bay, Sidney, B. C.
Foster, T. D. (1983), The temperature and salinity fine structure of the ocean under the Ross Ice Shelf (1983), *J. Geophys. Res.*, *88*, 2556–2564.
Gilmour, A. E. (1979), Ross Ice Shelf sea temperatures, *Science*, *203*, 438–439, doi:10.1126/science.203.4379.438.
Harder, M., and H. Fischer (1999), Sea ice dynamics in the Weddell Sea simulated with an optimized model, *J. Geophys. Res.*, *104*, 11,151–11,162.
Hellmer, H. H., F. Kauker, R. Timmermann, J. Determann, and J. Rae (2012), 21st-century warming of a large Antarctic ice shelf cavity by a redirected coastal current, *Nature*, *485*(7397), 225–228, doi:10.1038/nature11064.
Holland, D. M., and A. Jenkins (1999), Modeling thermodynamic ice-ocean interactions at the base of an ice shelf, *J. Phys. Oceanogr.*, *29*, 1787–1800.
Holland, D. M., S. S. Jacobs, and A. Jenkins (2003), Modelling the ocean circulation beneath the Ross Ice Shelf, *Antarct. Sci.*, *15*(1), 13–23, doi:10.1017/S0954102003001019.
Horgan, H. J., R. T. Walker, S. Anandakrishnan, and R. B. Alley (2011), Surface elevation changes at the front of the Ross Ice Shelf: Implications for basal melting, *J. Geophys. Res.*, *116*, C02005, doi:10.1029/2010JC006192.
Jacobs, S. S., A. L. Gordon, and J. L. Ardai Jr. (1979), Circulation and melting beneath the Ross Ice Shelf, *Science*, *203*, 439–443, doi:10.1126/science.203.4379.439.
Jenkins, A., H. F. J. Corr, K. W. Nicholls, C. L. Stewart, and C. S. M. Doake (2006), Interactions between ice and ocean observed with phase-sensitive radar near an Antarctic ice-shelf grounding line, *J. Glaciol.*, *52*(178), 325–346.
Joughin, I., and L. Padman (2003), Melting and freezing beneath Filchner-Ronne Ice Shelf, Antarctica, *Geophys. Res. Lett.*, *30*(9), 1477, doi:10.1029/2003GL016941.
Joughin, I., B. Smith, I. Howat, T. Scambos, and T. Moon (2010), Greenland flow variability from ice-sheet-wide velocity mapping, *J. Glaciol.*, *56*(197), 415–430.
King, M. A., L. Padman, K. Nicholls, P. J. Clarke, G. H. Gudmundsson, B. Kulessa, and A. Shepherd (2011a), Ocean tides in the Weddell Sea: New observations on the Filchner-Ronne and Larsen C ice shelves and model validation, *J. Geophys. Res.*, *116*, C06006, doi:10.1029/2011JC006949.
King, M. A., L. Padman, K. Nicholls, P. J. Clarke, G. H. Gudmundsson, B. Kulessa, A. Shepherd, and N. Gourmelen (2011b), Correction to "Ocean tides in the Weddell Sea: New observations on the Filchner-Ronne and Larsen C ice shelves and model validation," *J. Geophys. Res.*, *116*, C08026, doi:10.1029/2011JC007463.
Lewis, E. L., and R. G. Perkin (1986), Ice pumps and their rates, *J. Geophys. Res.*, *91*, 11,756–11,762, doi:10.1029/JC091iC10p11756.
Ligtenberg, S. R. M., M. M. Helsen, and M. R. van den Broeke (2011), An improved semi-empirical model for the densification of Antarctic firn, *Cryosphere*, *5*, 809–819, doi:10.5194/tc-5195-5809-2011.
Lorenz, E. N. (1956), Empirical orthogonal functions and statistical weather prediction, *Rep. 1*, pp. 49, Statistical Forecasting Project, Dep. of Meteorol., Mass. Inst. of Technol., Cambridge, Mass.
Lythe, M. B., D. G. Vaughan, and the BEDMAP Consortium (2001), BEDMAP: A new ice thickness and subglacial topographic model of Antarctica, *J. Geophys. Res.*, *106*, 11,335–11,351.
MacAyeal, D. R. (1984a), Thermohaline circulation below the Ross Ice Shelf: A consequence of tidally induced vertical mixing and basal melting, *J. Geophys. Res.*, *89*, 597–606, doi:10.1029/JC089iC01p00597.
MacAyeal, D. R. (1984b), Numerical simulations of the Ross Sea tides, *J. Geophys. Res.*, *89*, 607–615, doi:10.1029/JC089iC01p00607.
MacAyeal, D. R. (1985), Tidal rectification below the Ross Ice Shelf, Antarctica, *Antarct. Res. Ser.*, *43*, 109–132.
Mack, S., L. Padman, and J. Klinck (2013), Extracting tidal variability of sea ice concentration from AMSR-E passive microwave single-swath data: A case study of the Ross Sea, *Geophys. Res. Lett.*, *40*, 547–552, doi:10.1002/grl.50128.
Mahoney, A. R., A. J. Gough, P. J. Langhorne, N. J. Robinson, C. L. Stevens, M. J. M. Williams, and T. G. Haskell (2011), The seasonal appearance of ice shelf water in coastal Antarctica and its effect on sea ice growth, *J. Geophys. Res.*, *116*, C11032, doi:10.1029/2011JC007060.
Makinson, K., P. R. Holland, A. Jenkins, K. W. Nicholls, and D. M. Holland (2011), Influence of tides on melting and freezing beneath Filchner-Ronne Ice Shelf, Antarctica, *Geophys. Res. Lett.*, *38*, L06601, doi:10.1029/2010GL046462.
McPhee, M. G., C. Kottmeier, and J. H. Morison (1999), Ocean heat flux in the Central Weddell Sea during winter, *J. Phys. Oceanogr.*, *29*, 1166–1179, doi:10.1175/1520-0485(1999)029<1166:OHFITC>2.0.CO;2.
Mueller, R. D., L. Padman, M. S. Dinniman, S. Y. Erofeeva, H. A. Fricker, and M. A. King (2012), Impact of tide-topography interactions on basal melting of Larsen C Ice Shelf, Antarctica, *J. Geophys. Res.*, *117*, C05005, doi:10.1029/2011JC007263.
Naish, T., et al. (2009), Obliquity-paced Pliocene West Antarctic ice sheet oscillations, *Nature*, *458*(7236), 322–328.
Obukhov, A. M. (1947), Statistical homogeneous fields on a sphere, *Usp. Mat. Navk.*, *2*, 196–198.
Orsi, A. H., and C. L. Wiederwohl (2009), A recount of Ross Sea waters, *Deep Sea Res., Part II*, *56*, 13–14, doi:10.1016/j.dsr2.2008.10.033.
Padman, L., H. Fricker, R. Coleman, S. Howard, and S. Erofeeva (2002), A new tidal model for the Antarctic ice shelves and seas, *Ann. Glaciol.*, *34*, 247–254, doi:10.3189/172756402781817752.
Padman, L., S. Erofeeva, and I. Joughin (2003), Tides of the Ross Sea and Ross Ice Shelf cavity, *Antarct. Sci.*, *15*, 31–40, doi:10.1017/S0954102003001032.
Padman, L., L. Erofeeva, and H. A. Fricker (2008), Improving Antarctic tide models by assimilation of ICESat laser altimetry over ice shelves, *Geophys. Res. Lett.*, *35*, L22504, doi:10.1029/2008GL035592.
Padman, L., S. L. Howard, A. Orsi, and R. Muench (2009), Tides of the northwestern Ross Sea and their impact on dense outflows of Antarctic Bottom Water, *Deep Sea Res., Part II*, *56*, 818–834, doi:10.1016/j.dsr2.2008.10.026.
Padman, L., et al. (2012), Oceanic controls on the mass balance of Wilkins Ice Shelf, Antarctica, *J. Geophys. Res.*, *117*, C01010, doi:10.1029/2011JC007301.
Pawlowicz, R., R. Beardsley, and S. Lentz (2002), Classical tidal harmonic analysis including error estimates in MATLAB using T-TIDE, *Comput. Geosci.*, *28*, 929–937.
Pillsbury, R. D., and S. S. Jacobs (1985), Preliminary observations from long-term current meter moorings near the Ross Ice Shelf, Antarctica, *Antarct. Res. Ser.*, *43*, 87–107.
Pollard, D., and R. M. DeConto (2009), Modelling West Antarctic ice sheet growth and collapse through the past five million years, *Nature*, *458*, 329–332, doi:10.1038/nature07809.
Pritchard, H. D., S. R. M. Ligtenberg, H. A. Fricker, D. G. Vaughan, M. R. van denBroeke, and L. Padman (2012), Antarctic ice-sheet loss driven by basal melting of ice shelves, *Nature*, *484*, 502–505, doi:10.1038/nature10968.

Rignot, E., J. Mouginot, and B. Scheuchl (2011), Ice flow of the Antarctic ice sheet, *Science*, *333*(6048), 1427–1430.
Rignot, E., S. Jacobs, J. Mouginot, and B. Scheuchl (2013), Ice-shelf melting around Antarctica, *Science*, *341*(6143), 266–270, doi:10.1126/science.1235798.
Robinson, N. J., M. J. M. Williams, P. J. Barrett, and A. R. Pyne (2010), Observations of flow and ice ocean interactions beneath McMurdo Ice Shelf, Antarctica, *J. Geophys. Res.*, *115*, C03025, doi:10.1029/2008JC005255.
Scambos, T. A., J. A. Bohlander, C. A. Shuman, and P. Skvarca (2004), Glacier acceleration and thinning after ice shelf collapse in the Larsen B embayment, Antarctica, *Geophys. Res. Lett.*, *31*, L18402, doi:10.1029/2004GL020670.
Scambos, T. A., T. M. Haran, M. A. Fahnestock, T. H. Painter, and J. Bohlander (2007), MODIS-based Mosaic of Antarctica (MOA) data sets: Continent-wide surface morphology and snow grain size, *Rem. Sens. Environ.*, *111*(2), 242–257, doi:10.1016/j.rse.2006.12.020.
Shabtaie, S., and C. R. Bentley (1987), West Antarctic ice streams draining into the Ross Ice Shelf: Configuration and mass balance, *J. Geophys. Res.*, *92*, 1311–1336.
Shchepetkin, A. F., and J. C. McWilliams (2005), The Regional Oceanic Modeling System (ROMS): A split-explicit, free-surface, topography-following-coordinate oceanic model, *Ocean Modell.*, *9*(4), 347–404, doi:10.1016/j.ocemod.2004.08.002.
Shepherd, A., D. Wingham, D. Wallis, K. Giles, S. Laxon, and A. V. Sundal (2010), Recent loss of floating ice and the consequent sea level contribution, *Geophys. Res. Lett.*, *37*, L13503, doi:10.1029/2010GL042496.
Shepherd, A., et al. (2012), A reconciled estimate of ice-sheet mass balance, *Science*, *338*(6111), 1183–1189, doi:10.1126/science.1228102.
Stanton, T. P., W. J. Shaw, M. Truffer, H. F. J. Corr, L. E. Peters, K. L. Riverman, R. Bindschadler, D. M. Holland, and S. Anandakrishnan (2013), Channelized ice melting in the ocean boundary layer beneath Pine Island Glacier, Antarctica, *Science*, *341*(6151), 1236–1239.
Stern, A. A., S. W. Tyler, V. Zagorodnov, M. S. Dinniman, and D. M. Holland (2013), Intrusion of warm surface water beneath the McMurdo Ice Shelf, Antarctica, *J. Geophys. Res.*, *108*, 7036–7048, doi:10.1002/2013JC008842.
Tyler, S. W., D. M. Holland, V. Zagordnov, A. A. Stern, S. Kobs, S. White, F. Suarez, and J. Bryenton (2013), Using distributed temperature sensors to monitor an Antarctic ice shelf and sub-ice-shelf cavity, *J. Glaciol.*, *59*(215), 583–591, doi:10.3189/2013JoG12J207.